ACS NANO

www.acsnano.org

ARTICLE

Energy-Looping Nanoparticles: Harnessing Excited-State Absorption for Deep-Tissue Imaging

Elizabeth S. Levy,[†,⊥] Cheryl A. Tajon,[†,⊥] Thomas S. Bischof,[†] Jillian Iafrati,[‡] Angel Fernandez-Bravo,[†] David J. Garfield,[†,§] Maysamreza Chamanzar,[∥,▽] Michel M. Maharbiz,[∥] Vikaas S. Sohal,[‡] P. James Schuck,[†] Bruce E. Cohen,[†] and Emory M. Chan*[,†]

[†]The Molecular Foundry, Lawrence Berkeley National Laboratory, Berkeley, California 94720, United States

[‡]Department of Psychiatry, University of California, San Francisco, California 94143, United States

[§]Department of Chemistry and [∥]Department of Electrical Engineering and Computer Science, University of California, Berkeley, California 94720, United States

Supporting Information

ABSTRACT: **Near infrared (NIR) microscopy enables noninvasive imaging in tissue, particularly in the NIR-II spectral range (1000−1400 nm) where attenuation due to tissue scattering and absorption is minimized. Lanthanide-doped upconverting nanocrystals are promising deep-tissue imaging probes due to their photostable emission in the visible and NIR, but these materials are not efficiently excited at NIR-II wavelengths due to the dearth of lanthanide ground-state absorption transitions in this window. Here, we develop a class of lanthanide-doped imaging probes that harness an energy-looping mechanism that facilitates excitation at NIR-II wavelengths, such as 1064 nm, that are resonant with excited-state absorption transitions but not ground-state absorption. Using computational methods and combinatorial screening, we have identified Tm^{3+}-doped $NaYF_4$ nanoparticles as efficient looping systems that emit at 800 nm under continuous-wave excitation at 1064 nm. Using this benign excitation with standard confocal microscopy, energy-looping nanoparticles (ELNPs) are imaged in cultured mammalian cells and through brain tissue without autofluorescence. The 1 mm imaging depths and 2 μm feature sizes are comparable to those demonstrated by state-of-the-art multiphoton techniques, illustrating that ELNPs are a promising class of NIR probes for high-fidelity visualization in cells and tissue.**

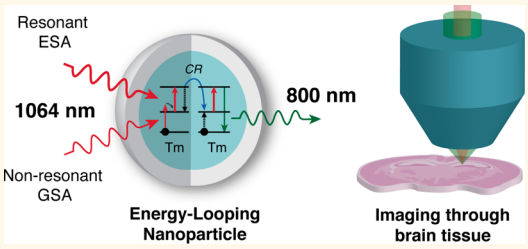

KEYWORDS: *energy looping, photon avalanche, upconversion, nanocrystals, nanoparticles, near-infrared, imaging*

Optical imaging using near-infrared (NIR) light is a promising technique for imaging biological processes deep within tissue due to the radiation's low energies and minimal propensity to excite autofluorescence.[1,2] In contrast to visible light, the low scattering and absorption of NIR photons by typical tissues (*e.g.*, brain, Figure 1a) enables imaging of micron-scale features through millimeters of sample.[1] Much of the recent exploration of NIR imaging has focused on the NIR-II window; the 1000−1400 nm region of the spectrum (Figure 1a) that exhibits high transmission in tissue.[3−5] Existing NIR-II probes, including organic dyes,[3] carbon nanotubes,[4,6] and semiconductor nanoparticles,[5] have enabled *ex vivo* and *in vivo* imaging of mouse vasculature and internal organs through skin, tissue, and skull. Radiation at these wavelengths and fluences (up to 10^6 W/cm^2) is sufficiently benign such that red blood cells have been optically trapped in living mice without tissue damage,[7] and *E. coli* and yeast cells have been observed dividing within 1064 nm traps.[8]

In this work, we develop a class of materials, called energy-looping nanoparticles (ELNPs), that we designed specifically for imaging in deep tissue at NIR-II wavelengths (*i.e.*, 1064 nm). This looping process (Figure 1b) occurs in nanoparticles doped with selected compositions of lanthanide ions. In general, lanthanide-doped nanoparticles are attractive alternatives[2] to existing NIR probes because they can offer high photochemical stability,[9] low-toxicity compositions,[10] large Stokes and anti-Stokes shifts, and narrow spectral features.[11] NIR radiation can excite $4f^N \rightarrow 4f^N$ transitions in lanthanide-doped nanocrystals to produce both Stokes[2] and upconverted emission.[11−13] The emission wavelength can be tuned precisely by controlling the combination[14] and partitioning[15] of dopants.[13]

Received: May 18, 2016
Accepted: September 1, 2016
Published: September 7, 2016

DOI: 10.1021/acsnano.6b03288
ACS Nano 2016, 10, 8423−8433

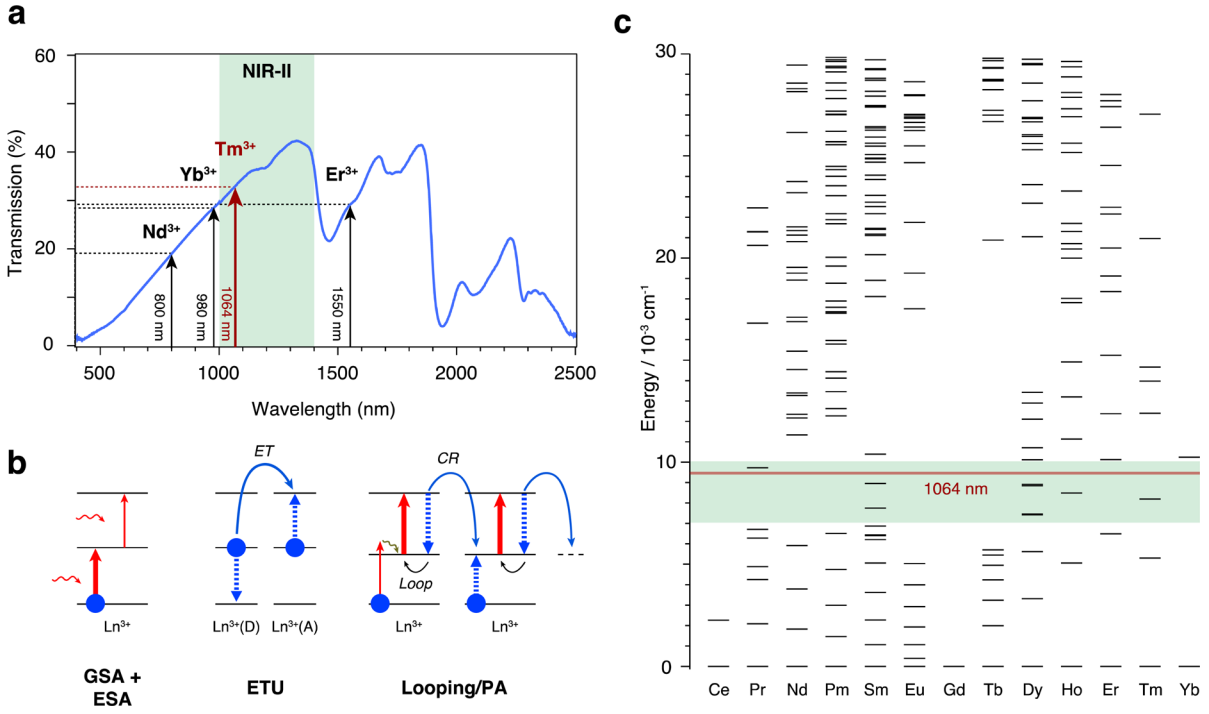

Figure 1. (a) **Transmission spectrum through the frontal cortex of a 1 mm-thick, fixed coronal brain slice from an adult mouse (see Methods for experimental details). Common NIR excitation wavelengths of Nd^{3+}, Yb^{3+}, and Er^{3+} are superimposed, along with the 1064 nm looping excitation line of Tm^{3+} (this work) and the NIR-II window between 1000 and 1400 nm. (b) Three mechanisms of upconversion in lanthanide ions: ground-state absorption (GSA) followed by excited-state absorption (ESA), energy-transfer upconversion (ETU), and looping/photon avalanche (PA). Thickness of arrows increases with rate. Blue circles indicate individual ions occupying a given state. (c) $4f^N$ energy manifolds of trivalent lanthanide ions in vacuum, with NIR-II window and 1064 nm laser line superimposed.**

These luminescence processes typically require that sensitizing dopants have strong ground-state absorption (GSA) transitions that are resonant with the excitation energy (Figure 1b). This requirement restricts excitation to a small set of discrete NIR wavelengths (*e.g.*, 800 nm,[16,17] 980 nm,[11,18] and 1550 nm,[19] as in Figure 1a) that fall outside the ideal NIR-II window for imaging in tissue, leading to excessive scattering, photodamage, or sample heating.[17,20,21] Lanthanide electronic structure diagrams suggest that there are numerous GSA transitions with energies in the 1000−1400 nm window (Figure 1c), but there are few reports of lanthanide-doped materials that exhibit efficient luminescence when excited resonantly at 1064 nm or other common NIR-II laser lines.

Seeking materials that could be excited in the NIR-II window, we explored an alternate approach leveraging the absorption of photons by lanthanide excited states. Excited-state absorption (ESA) rates, however, are typically low relative to GSA since the populations of excited states are often 10 orders of magnitude lower than the ground state.[12]

A photophysical phenomenon known as energy looping[11,22−24] provides a strategy for populating excited states in the absence of strong GSA. Looping amplifies the population of an intermediate excited state *I* through a positive feedback loop of ESA from *I*, followed by cross relaxation (CR, Figure 1b) back down to *I*. Each CR event produces two ions in the *I* state for every photon absorbed. These two ions can absorb two more photons to generate four intermediate states (Figure 1b). Repeated looping cycles amplify the population of *I* nonlinearly, dramatically increasing the material's absorptivity. Since weak GSA can seed the small populations of *I* necessary to initiate this process, looping could enable upconversion from NIR-II wavelengths that are not resonant with ground-state transitions of dopants in the nanoparticles.

Only a few nanoparticle systems have definitively demonstrated looping, primarily to access the extreme form of looping known as photon avalanche,[25−27] (PA), and none have been leveraged for biological imaging. Looping mechanisms are the product of complex networks of energy transfer between dopant ions;[24] therefore, energy-looping compositions are not easily identified by cursory analysis of lanthanide energy levels or by trial-and-error experimentation. In prior work, we directed and accelerated the exploration of lanthanide compositional space by establishing a high-throughput pipeline[12,14,28] for the theoretical prediction and experimental validation of upconverting nanoparticles (UCNPs) with brighter[18] and more spectrally pure emission.[14,29]

In this work, we used computational modeling and combinatorial screening to identify dopant compositions that exhibit efficient looping and upconversion from biologically benign 1064 nm light. These screens revealed Tm^{3+}-doped $NaYF_4$ ELNPs that are excited efficiently at 1064 nm and emit at 800 nm. The 1064 nm excitation wavelength lies in the ideal NIR-II range for multiphoton excitation in highly scattering tissue, while the upconverted emission of Tm^{3+} at 800 nm enables imaging using standard silicon detectors. To demonstrate the penetration depths accessible by 1064 nm excitation, we used ELNPs to image features as small as 2 μm through 1 mm of fixed mouse brain tissue. We also performed confocal microscopy of ELNPs in cultured mammalian cells, demonstrating that autofluorescence-free luminescence imaging of cells can be performed using continuous-wave (cw) excitation at 1064 nm, which has not been extensively investigated.[30] Our screening methods provide a viable path for further exploration

DOI: 10.1021/acsnano.6b03288
ACS Nano 2016, 10, 8423−8433

of ELNPs active at NIR wavelengths, facilitating the imaging and stimulation of biological processes currently obscured by scattering and absorption.

RESULTS AND DISCUSSION

High-Throughput Computational Screening. To identify lanthanide dopant compositions that exhibit nonresonant upconversion when excited in the NIR-II window, we used a high-throughput computational method that we have developed to predict brighter dopant compositions for imaging single UCNPs[18] and to explain the mechanisms of spectral purity in codoped upconverting nanoparticles.[14,29] These differential rate equation calculations deterministically solve the populations of each lanthanide $4f^N$ manifold using rate constants derived from Judd–Ofelt theory[31] and other photophysical models.[12] For this work we explored materials that can be excited at 1064 nm, since this is a common laser wavelength[30,32] and falls within the NIR-II window.

To begin, we calculated the upconverted luminescence spectra of β-$NaYF_4$ doped with every combination of one, two, and three distinct lanthanide dopants (out of 10, excluding La^{3+}, Ce^{3+}, Pr^{3+}, Pm^{3+}, and Lu^{3+}), with each dopant comprising one atomic percent of the rare-earth content of the nanoparticle. The intensity of each composition was characterized by its emission rate (photons/s) integrated from 300 to 900 nm under 1064 nm excitation (10^5 W/cm^2). Nanoparticles containing Tm^{3+} exhibited the highest rates of upconverted luminescence (Figure 2a) and among the highest rates of absorption at 1064 nm. Codoping these nanoparticles with additional ions did not enhance the emission, which is dominated by the Tm^{3+}: $^3H_4 \rightarrow {}^3H_6$ transition at 800 nm. Materials sensitized with Yb^{3+} were also predicted to absorb 1064 nm excitation in the absence of Tm^{3+}, but the emission intensities of Yb^{3+}-sensitized UCNPs were calculated to be an order of magnitude lower than Tm^{3+}-doped nanoparticles due to the requirement of phonon assistance. Codoping Yb^{3+} with Tm^{3+} did not increase emission relative to UCNPs doped with Tm^{3+} only (Figure 2a).

The emergence of Tm^{3+}-doped nanoparticles as the brightest emitters under 1064 nm excitation was unexpected, since their calculated energy levels cannot host ground-state transitions resonant with 1064 nm light. Reported absorption spectra for Tm^{3+}-doped materials[33,34] measured under fluxes characteristic of typical spectrophotometers show no absorption peak at this wavelength (reproduced in Figures S1 and S2). The minimal GSA occurs through the high-energy tail, or phonon sideband, of the Tm^{3+}:$^3H_6 \rightarrow {}^3H_5$ GSA peak centered at 1200 nm. We calculated absorption cross sections at 1064 nm ($\sigma_{1064} \sim 5 \times 10^{-23}$ cm^2) that were 100-fold smaller than the peak values at 1200 nm. The low absorption at 1064 nm,consistent with experimental cross sections below 1×10^{-22} cm^2,[33,34] may explain why there are few reports of upconversion in Tm^{3+}-doped materials excited at 1064 nm[34−36] and none describing colloidal nanoparticles.

Experimental Validation. To resolve this discrepancy between our predicted results and the dearth of reports observing 1064 nm absorption in Tm^{3+}, we synthesized a library of β-$NaYF_4$ nanoparticles doped with Tm^{3+} concentrations ranging from 0.1 to 1.5 at %.[9] Although Gd^{3+} does not actively enhance the optical properties of Tm^{3+}-doped ELNPs, we codoped them with 20% Gd^{3+} to ensure growth in the hexagonal β-phase of $NaYF_4$ rather than in the less efficient cubic phase.[28,37] NIR absorption spectra of these nanoparticles

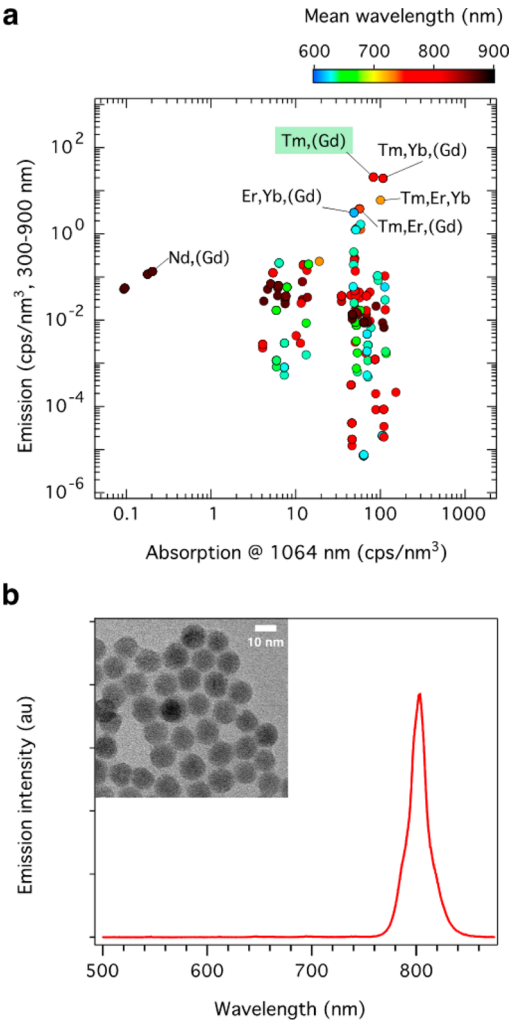

Figure 2. (a) High-throughput computational screening of singly, doubly, and triply doped $NaYF_4$ with the concentration of each lanthanide dopant fixed at 1 at %. Calculated emission intensity, integrated between 300 and 900 nm, is plotted *vs* absorption at 1064 nm (10^5 W/cm^2). Colors represent the mean weighted wavelength for the 300–900 nm emission range. Elements in parentheses denote optional dopants that do not affect the outcome for these compositions. (b) Experimental upconversion luminescence spectra of $NaYF_4$:20% Gd^{3+}, 0.5% Tm^{3+} nanoparticles excited at 1064 nm (5×10^5 W/cm^2). Inset: transmission electron micrograph of the measured nanoparticles.

did not exhibit discernible absorption at 1064 nm. At 1064 nm illumination below 10^3 W/cm^2, characteristic of ensemble measurements in benchtop spectrometers, no upconverted emission was detected. However, at excitation fluxes $>3 \times 10^3$ W/cm^2 in a confocal microscope, the particles produced upconverted emission at 800 nm characteristic of Tm^{3+}: $^3H_4 \rightarrow {}^3H_6$ electric dipole radiation (Figure 2b), as predicted by calculations. The strong dependence of the emission on the excitation power, shown in Figure 3a, may explain the dearth of reports on this system outside of lasing studies.

Mechanistic Analysis of Looping. We sought to elucidate a mechanism for the nonresonant excitation of upconverted emission in Tm^{3+}:$NaYF_4$. The emission intensity I exhibited a high dependence on laser power density (P) with the slope of the log I *vs* log P plot increasing from 2.6 ± 0.2 to 3.2 ± 0.2 before saturating at a slope of 0.95 ± 0.02 (Figure 3a). The

DOI: 10.1021/acsnano.6b03288
ACS Nano 2016, 10, 8423–8433

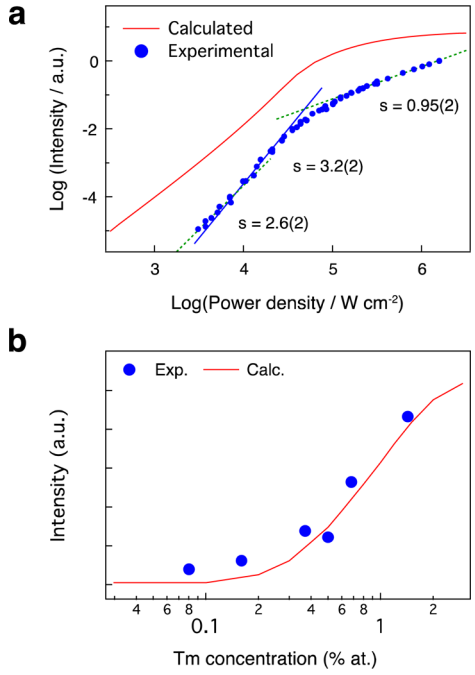

Figure 3. (a) Dependence of the 800 nm upconverted luminescence from 0.5% Tm^{3+} ELNPs on excitation power density at 1064 nm. Slopes are marked on experimental data, with the numeral in parentheses indicating the standard deviation of the last digit. (b) Dependence of emission intensity on Tm^{3+} concentration at 10^5 W/cm^2 power density.

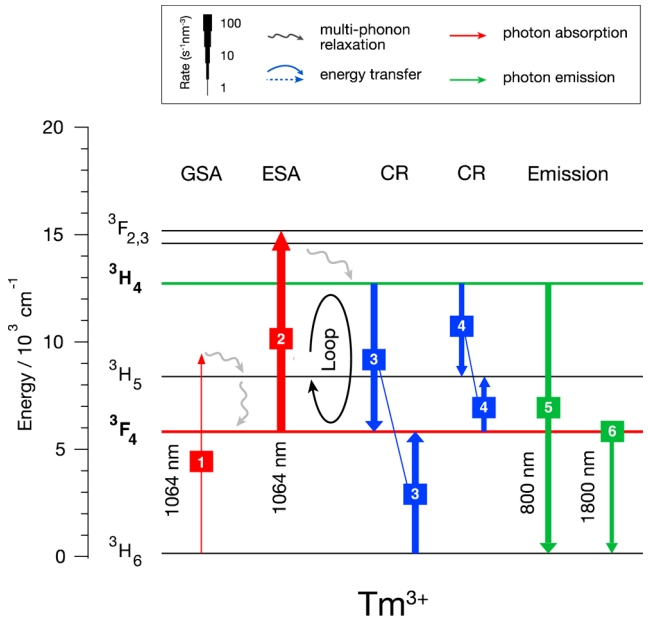

Figure 4. Looping mechanism in Tm^{3+}-doped $NaYF_4$. Energy levels represent $4f^{12}$ manifolds of Tm^{3+}. Arrows are manifold-to-manifold transitions as described in the legend. The thickness of the arrows varies logarithmically with the rate of the transition at steady state, as calculated for 1% Tm^{3+} at 1064 nm excitation (10^5 W/cm^2).

sigmoidal power dependence suggests a mechanism that is more complex than traditional, two-photon upconversion mechanisms involving sequential GSA/ESA or ETU (Figure 1b).[11] Since the combined energy of two or more, 1064 nm photons significantly exceeds the energy necessary to upconvert them to an 800 nm photon, a slope near three indicates that rapid, nonradiative processes such as cross-relaxation must be competing with radiative pathways. The increasing emission intensity with Tm^{3+} concentration (Figure 3b) further suggests a mechanism dependent on energy transfer between Tm^{3+} ions. This combination of nonresonant GSA, strong power dependence, and reliance on energy transfer led us to hypothesize a mechanism involving moderate looping.

To quantitatively derive this looping mechanism, we returned to our rate equation calculations, whose power dependence and concentration dependence trends are qualitatively consistent with experimental data (Figure 3). We reconstructed the critical pathway for the upconverted emission in Tm^{3+}:$NaYF_4$ by recursively tracing the transitions that contribute to the population (at least 80%) of the 800 nm emitting state.[29] This computational analysis, calculated at 10^5 W/cm^2 excitation and 1% Tm^{3+}, produced the quantitative steady-state mechanism shown in Figure 4 (rates are depicted by the thickness of the arrows and are given in Table S4). In the critical pathway, a weak, off-resonant GSA transition (step 1 in Figure 4) is followed by a resonant ESA transition to the $^2F_{2,3}$ manifolds (step 2, identified in the text as ESA2). Since the $^3F_4 \rightarrow {}^3F_2$ ESA transition is resonant at 1064 nm, it proceeds at roughly 50 times the rate of GSA.

Following multiphonon relaxation (MPR) to the $^3H_4$ manifold, one Tm^{3+} ion can cross-relax by donating energy partially to a second Tm^{3+} ion in its ground state (step 3, or CR3), resulting in *two* Tm^{3+} ions in their intermediate $^3F_4$ state. Each of these two ions can repeat the ESA2-CR3 "loop" multiple times. In theory, the population of the $^3F_4$ manifold doubles with each looping cycle, explaining the inversion of the steady-state $^3F_4$ and $^3H_6$ populations (Figure S3).

If the population of the Tm^{3+}:$^3F_4$ manifold did increase exponentially, the mechanism depicted in Figure 4 would be considered a photon avalanche (PA) process. A process is classified as PA when the ratio of the ESA and GSA rate constants, $R = A_{GSA}/A_{ESA}$, lies below a critical value of $R_{max} = 10^{-4}$.[38] For Tm^{3+}-doped materials excited at 1064 nm, PA behavior has only been observed in bulk materials at cryogenic temperatures.[39]

At ambient or elevated temperatures, Tm^{3+}-doped $NaYF_4$ nanoparticles excited at 1064 nm exhibit $R \sim 0.02$. Since $R > R_{max}$, we attribute the upconversion of 1064 nm light in these materials to looping. Unlike in PA, the looping cycle in Tm^{3+}-doped ELNPs experiences significant losses, most notably through radiative relaxation from the $^3H_4$ to the $^3H_6$ manifold, emitting upconverted light at 800 nm (step 5, Figure 4). Additional energy leaks out of the energy loop via cross relaxation in step 4 and radiative relaxation in step 6 (Figure 4). These energy leaks result in subexponential growth with each ESA2-CR3 loop. The moderate looping ($R \sim 0.02$) provides a rationalization for the subtle increase in the slope of the power dependence (Figure 3a), rather than a more abrupt sigmoidal curve indicative of PA.[39,40]

To highlight the dominant role of looping in this upconversion mechanism, we discuss relative probabilities of transitions in terms of a total branching ratio β', which is the ratio of the rate of a process to the aggregate rate of all photophysical processes that originate from the same manifold[29] (see additional analytical methods in the Supporting Information). For transitions originating from the $^3H_4$ manifold, the CR3 step responsible for looping has $\beta'_{CR3} = 0.35$, the most probable relaxation pathway from this manifold. Physically, this means that for every 100 ions occupying a $^3H_4$

DOI: 10.1021/acsnano.6b03288
ACS Nano 2016, 10, 8423–8433

manifold under steady-state conditions, 35 will relax via CR3 and increase the population of the $^3F_4$ manifold by 70 ions. Radiative emission (Em5) is the next most likely transition with a β'_{Em5} = 0.22. The CR3 cross-relaxation is so dominant at steady state that it, not GSA, accounts for 85% of the transitions involving the ground state. 62% of all transitions from the intermediate $^3F_4$ "reservoir" state are ESA, highlighting the power of the looping cycle to promote excited-state transitions. We note that it is the unique electronic structure of Tm^{3+} that fosters this balance of ESA, CR, and emission that is essential for hosting efficient looping at 1064 nm.

Quantum Yield. To quantify the efficiency of Tm^{3+}-doped ELNPs, we calculated their theoretical quantum yield (QY) from the excitation and emission rates output from our modeling. We previously used this method, detailed in the Supporting Information, to reproduce the experimental QY of Er^{3+}- and Yb^{3+}-doped UCNPs.[18,29] This theoretical approach is necessary since relative QY standards do not exist for upconversion of 1064 nm light, and since absolute quantum yields are difficult to measure experimentally at the photon fluxes required to induce looping. Our calculations (Table S5) reveal that, for bulk and highly passivated core−shell nanoparticles, the 800 nm emission from 1.5% Tm^{3+}-doped $NaYF_4$ exhibits a theoretical QY of 20% when excited with 1064 nm light at 10^5 W/cm^2. In practice, surface quenching reduces the QY of lanthanide-doped nanoparticles, a phenomenon that we modeled by incorporating nonemissive surface species that accept energy from emissive dopants.[18] For 8 nm ELNPs doped with 1 to 20% Tm^{3+}, we calculated quantum yields from 0.03 to 0.05% (Table S5). These QY values are comparable to values that we previously measured for 8 nm nanoparticles of the canonical $NaYF_4$:20% Yb^{3+}, 2% Er^{3+} upconverting material.[18] We anticipate that high-quality passivation of ELNPs with undoped shells will allow us to realize QYs that approach theoretical limits. We note that for biological imaging, the brightness, not QY, determines imaging speed and sensitivity. The overall emission intensity of Tm^{3+}-doped ELNPs exceeds that of any other lanthanide-doped system under 1064 nm excitation (Figure 2a), suggesting the utility of ELNPs for imaging cells and tissue.

Imaging ELNPs in Mammalian Cells. Live cells have commonly been manipulated with cw 1064 nm lasers, but rarely imaged[30] (two-photon microscopy[30] and photoacoustic experiments[41] that use 1064 nm typically use pulsed lasers). For optical imaging, excitation at NIR-II wavelengths and anti-Stokes NIR emission suggests the possibility of imaging with little or no phototoxicity or autofluorescent background. We sought to demonstrate that ELNPs could be deployed and unambiguously visualized inside cells with 1064 nm excitation. ELNPs (11 nm diameter; 1.5% Tm^{3+}) with 2 nm undoped shells[42,43] were first treated with mild acid to remove their native hydrophobic ligands[44] and then characterized by DLS to ensure the resulting aqueous dispersion did not contain aggregates (Figure S6). We examined these nanoparticles for signs of cytotoxicity using a luminescence assay that measures cell viability (Figure S8 and Methods). HeLa cells were incubated with ELNPs for 17 h for uptake by nonspecific endocytosis, and metabolic activity was measured relative to cells treated with a known apoptotic inducer, staurosporine (STS). ELNP-treated cells showed significant differences in viability compared to STS-treated cells ($p < 0.001$), but not to vehicle-only controls ($p > 0.05$). Following cell fixation, confocal microscopy and spectral images acquired with 1064 nm excitation and 800 nm emission show punctate patterns that correspond to endosomal staining with no discernible background (Figure 5). To confirm that this emission is due to

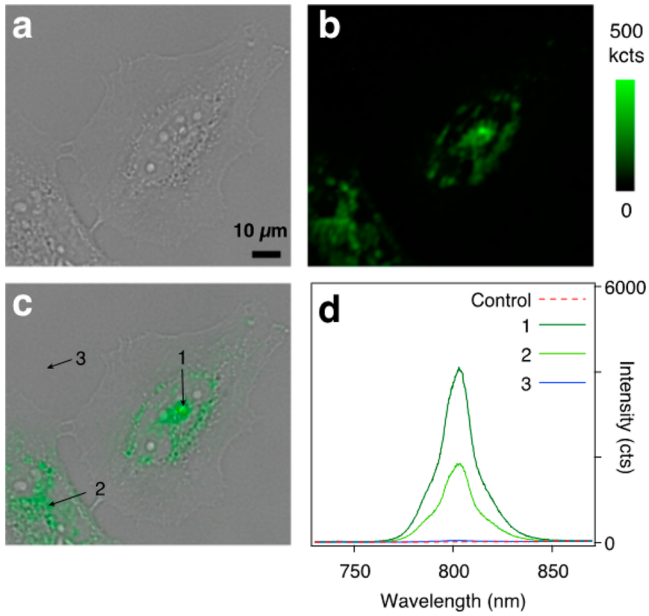

Figure 5. Confocal imaging of HeLa cells fixed after incubation with 1.5% Tm^{3+} ELNPs. Bright-field (a), luminescence integrated between 740 and 870 nm (b), and overlaid micrographs (c) under 1064 nm excitation (10^6 W/cm^2). Luminescence spectra (d) from numbered points in (c). Note the absence of measurable 800 nm emission outside of cell boundaries (3) and in a vehicle control lacking ELNPs (Figure S7).

the ELNPs and not two-photon autofluorescence, we treated a control population of HeLa cells with an identical procedure that excluded ELNPs, and no 800 nm signal above background could be detected (Figures 5d and S7).

These initial results illustrate the added leverage of ELNPs as biological labels that can be excited nondestructively at 1064 nm with no detectable autofluorescence. However, these materials will provide maximal biological utility when used to image live cells. Toward this end, we investigated the phototoxicity of 1064 nm exposure to determine the tolerance of live mammalian cells to long-term ELNP imaging (Figure 6). Cell tolerance to 10^6 W/cm^2, 1064 nm exposure was assayed in a time course using propidium iodide (PI), a DNA intercalating dye that exhibits 617 nm emission only when the cell membrane is compromised. Integrated PI emission intensities from HeLa cells imaged under 1064 nm excitation for up to 157 min exhibited no measurable difference from the PI emission of unimaged cells, with only autofluorescent background apparent (Figures 6 and S9). The 157 min maximum acquisition time corresponded to 43 min of actual exposure to 1064 nm excitation (see Supporting Information for live cell imaging methods). At exposure times longer than 43 min, HeLa cells began to exhibit PI emission, indicating initial signs of cellular distress (Figures 6f and S9d). While NIR excitation at these fluences is likely to generate some heat, there is precedent for imaging or trapping in the NIR without any observable hyperthermia.[7,45] The lack of observed phototoxicity in our experiments may arise from the *ca.* 20 °C difference between room temperature and the temperature threshold for cellular hyperthermia.[46] We also note that these PI assays offer

DOI: 10.1021/acsnano.6b03288
ACS Nano 2016, 10, 8423−8433

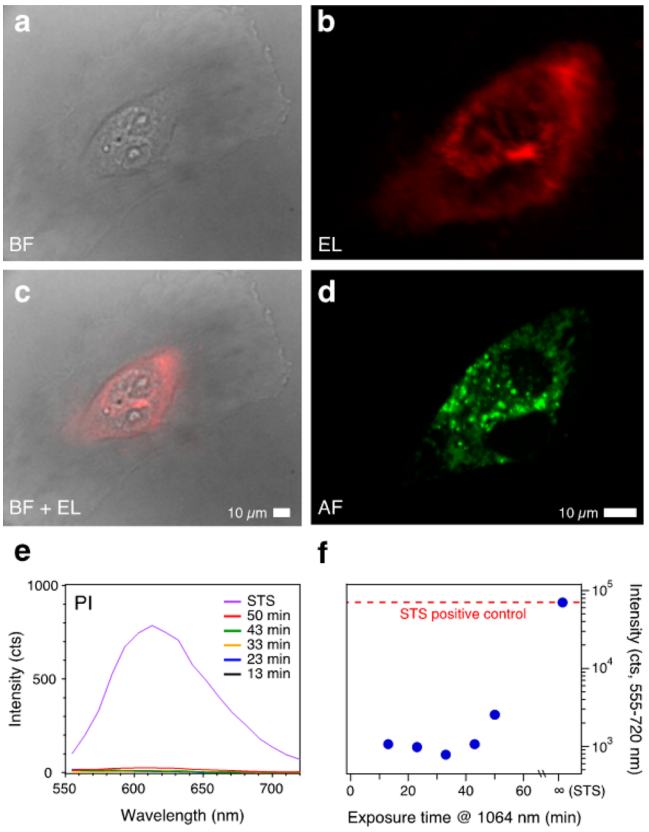

Figure 6. Confocal imaging of live HeLa cells after treatment with 1.5% Tm^{3+} ELNPs. Bright-field (a), luminescence integrated between 740 and 870 nm (b), and overlaid micrographs (c) under 1064 nm excitation (10^6 W/cm^2). (d) Micrograph of cellular autofluorescence excited at 488 nm following imaging over 23 min at 1064 nm. Scale bars are identical between (a) and (c) and between (b) and (d). Emission spectra (e) and integrated emission intensities (f) from PI-stained HeLa cells excited at 514 nm after five different exposures to 1064 nm excitation, or after exposure to 1 μM STS (positive control). Note the absence of measurable PI emission relative to the STS control, indicating cell viability even after exposure to 1064 nm excitation for up to 43 min. Emission micrographs of cells treated with PI (Figure S9) and STS (Figure S10) are shown in the Supporting Information.

a second, independent test of ELNP cytotoxicity, with no detectable effects on either membrane integrity or cell metabolism. These studies demonstrate that HeLa cells remain viable under the high excitation intensities required to image ELNPs in live cells (Figure 6). Since these exposure times (>30 min) exceed typical acquisition times for confocal microscopy of biological specimens, ELNPs may be applied to address biological questions that require examination over repeated or extended time scales.

Imaging through Deep Tissue and Other Scattering Media. Given the ability of Tm^{3+}-doped ELNPs to be excited in the NIR-II window, we reasoned that these energy-looping nanomaterials could be imaged with high resolution through highly scattering media. As discussed earlier, optical propagation loss in mouse brain tissue is significantly lower at 1064 nm compared to the loss at 800, 1550, and even 980 nm, suggesting that Tm^{3+}-doped ELNPs could be imaged at depths currently out of the range of UCNPs. To make a tissue-like medium that mimics the optical properties of brain tissue, we cast phantoms of 1% w/v agarose with 0−0.5% w/v Intralipid (IL) emulsion. By changing the concentration of agarose and IL, we could precisely control the optical propagation loss within the phantom gels. We did not incorporate visible dyes since the dominant mode of NIR attenuation in tissue is scattering and absorption by water or organic molecules. The transmission spectrum of these phantoms qualitatively matched that of fixed mouse brain (Figure 7a). Due to their scattering at visible wavelengths, 1 mm-thick phantoms with 0.25 to 0.5% IL appeared opaque (Figure 7b).

We sought to benchmark these ELNP probes by creating features that could be imaged systematically through different tissues and phantoms. We loaded polystyrene (PS) beads[47] (d = 5 μm) with core−shell ELNPs with 0.5% Tm^{3+}. The beads were dried on silicon dies and fixed in a rigid frame so that the same beads could be imaged reproducibly through a range of phantoms placed above the beads (Figure S11) and with the same excitation power. This method enabled us to definitively measure the impact of different phantoms and tissue on the attenuation of ELNP emission and the impact on the resolution of confocal imaging.

When imaging through 1 mm of phantom (0.25% IL), the ELNP-loaded beads could be resolved readily (Figure 7c) via scanning confocal microscopy with 1064 nm excitation and emission spectra collected around 800 nm. At the same excitation power at the microscope objective, the emission signal $S_{phantom}$ collected from beads excited and emitting through the phantom, was reduced to an average of $S_{phantom}/S_0$ = 36% of the emission signal S_0 from the beads collected with no phantom. This 64% reduction in signal is the consequence of the attenuation of the 1064 nm excitation as it passes through the phantom to the beads, combined with the attenuation of the 800 nm emission returning to the objective through the phantom.

To compare 1064 nm imaging with current state-of-the-art UCNPs, we used 785 nm excitation in the same confocal microscope to image 5 μm beads loaded with $NaYF_4$ nanoparticles doped with Nd^{3+}, Yb^{3+}, Ho^{3+}, and Gd^{3+} (20/10/2/20%) and coated with a $NaYF_4$:20% Gd^{3+} shell. At the same 10^6 W/cm^2 power density used for the ELNPs, these 785 nm-excited beads could still be resolved through the same, 1 mm thick phantom (Figures S12 and S13). However, the average $S_{phantom}/S_0$ ratios for the 540 and 640 nm emission peaks of these Nd^{3+}-sensitized UCNPs were only 2.8 and 7.4%, respectively (Figure 7e) or 5- to 13-fold less than for Tm^{3+}-doped ELNPs under 1 mm phantom. The larger $S_{phantom}/S_0$ ratio of ELNPs relative to UCNPs is due to the greater transmission of the ELNPs' NIR excitation and emission wavelengths through the phantom (Figure 7d). Since confocal imaging depths in tissue are predominantly limited by signal retention,[48] these results suggest that the maximum imaging depths of ELNPs under 1064 nm excitation may substantially exceed those of UCNPs.

Imaging through Brain Tissue. To demonstrate the ability to probe through actual, highly scattering tissue, we used confocal imaging of ELNPs at 1064 nm to perform high-resolution imaging through fixed coronal slices of adult mouse brain[49] (Figure 8a). We imaged the same constellation of ELNP-loaded beads through the frontal cortex of brain slices with thicknesses of 0.5 and 1.0 mm (thicknesses were measured before fixing). As shown in Figure 8b, the 5 μm beads were clearly resolved with 1064 nm confocal microscopy through the thickest mouse brain slice (1.0 mm). In contrast, the Nd^{3+}-sensitized beads excited at 785 nm could only be resolved

DOI: 10.1021/acsnano.6b03288
ACS Nano 2016, 10, 8423−8433

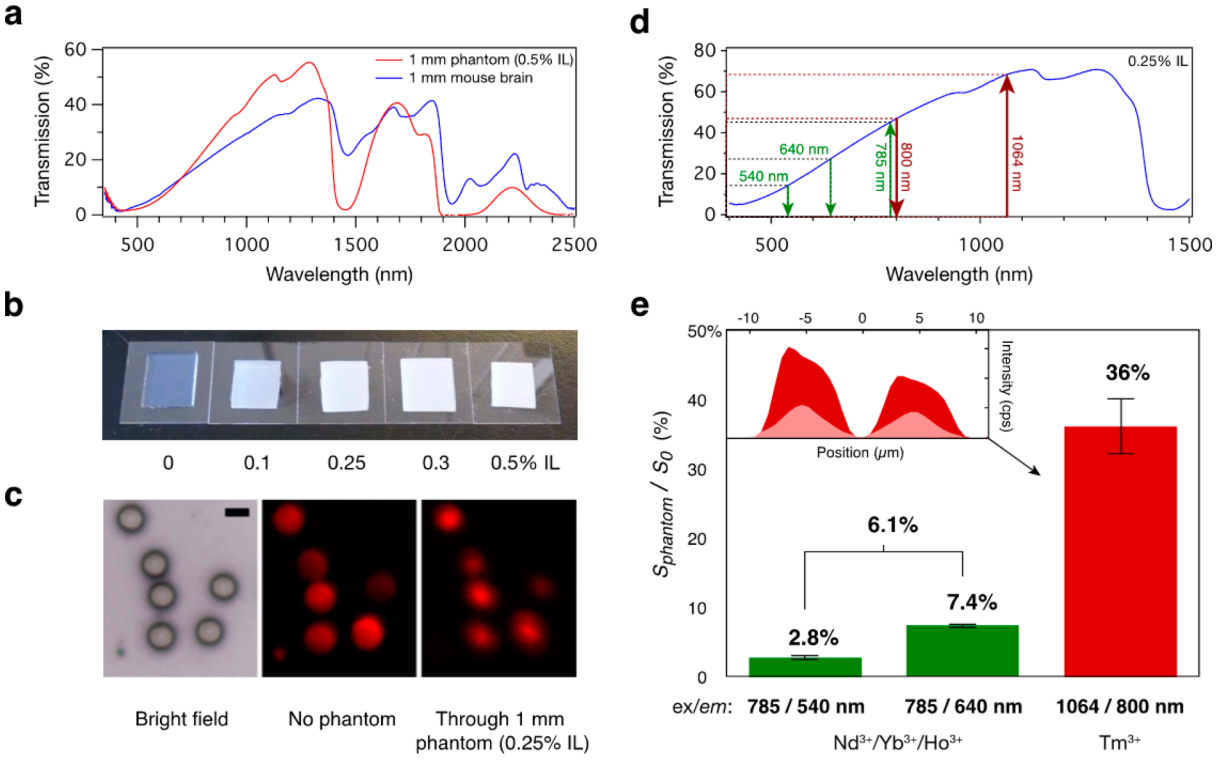

Figure 7. (a) Comparison of the transmission spectra of mouse brain and phantom (1% agarose, 0.5% IL). The thickness of both samples was 1 mm. (b) Photograph of phantoms at five IL concentrations. (c) Confocal luminescence micrographs of 5 μm PS beads loaded with 0.5% Tm^{3+} ELNPs imaged directly and through 1 mm of 0.25% IL phantom (1064 nm ex., 740−870 nm em.). (d) Transmission spectrum of the 0.25% IL phantom, superimposed with the excitation and emission wavelengths of Tm^{3+}-ELNPs (red) and $NaYF_4$:Gd^{3+}, Nd^{3+}, Yb^{3+}, Ho^{3+} UCNPs (20/20/10/2%) (green). (e) Comparison of intensities of beads loaded with Tm^{3+} ELNPs or Nd^3-sensitized UCNPs (785 nm ex., 540 and 640 nm em.) imaged through the 0.25% IL phantom. Relative intensities for each type of bead are reported as the ratio of the intensities ($S_{phantom}/S_0$) with and without the 1 mm phantom above the beads at 10^6 W/cm^2 excitation. Error bars represent standard deviation across N = 6 microbeads. Inset: Intensity line cuts for the two lowest beads in (c) when excited at 1064 nm with (pink) and without phantom (red).

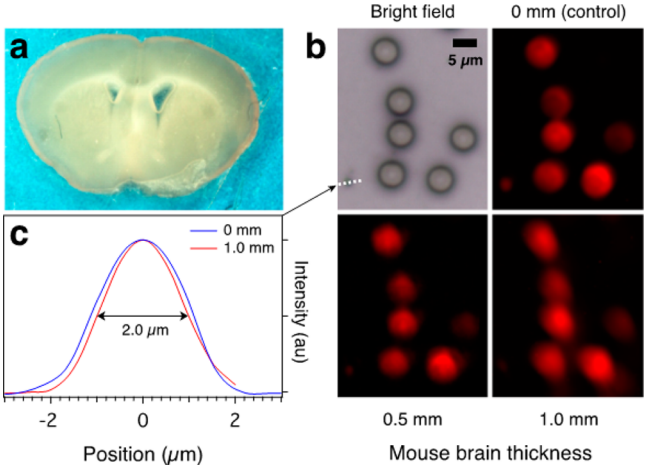

Figure 8. (a) Representative mouse brain slice through which ELNP beads were imaged. (b) Bright-field and confocal luminescence micrographs of Tm^{3+}-doped ELNP beads imaged through 0, 0.5, and 1 mm-thick brain slices (1064 nm ex., 10^6 W/cm^2). (c) Intensity line cuts of unbound ELNPs as measured along the white dashed line shown in (b), illustrating 2 μm resolution through 1 mm brain slices. A magnified view of this region is shown in Figure S15.

through 0.5 mm of brain tissue (Figure S14). No signal could be detected for the Nd^{3+}-sensitized UCNPs through 1.0 mm of mouse brain, thus a side-by-side comparison of Tm^{3+}-doped ELNPs and Nd^{3+}-sensitized UCNPs at this brain thickness was not possible.

Line cuts of a small cluster of ELNPs not associated with any microbeads (Figure 8c) show no evidence for loss of resolution through the brain slice when imaging with 1064 nm, consistent with prior multiphoton investigations in turbid media.[48] The fwhm of 2.0 μm at 1 mm imaging depth is comparable to fwhm values of 0.9 μm observed by Xu *et al.*[1] at similar depth (844 μm) using three-photon imaging with 1700 nm excitation. The 2.0 μm features observed with ELNPs through brain tissue are finer than capillaries in mouse brain ($d \approx 3$ μm).[1] Our results demonstrate the utility of ELNPs excited at 1064 nm both for high fidelity imaging through cells and also for deep brain imaging through at least 1 mm of tissue, at depths and feature sizes comparable to that of state-of-the-art multiphoton methods.

Discussion. In this work, we present a class of nanomaterials, ELNPs, that produce upconverted luminescence when excited at wavelengths far from their ground-state resonances. This phenomenon allows ELNPs to be imaged with NIR-II light in cells and deep tissue using commonly available cw lasers and standard silicon detectors. The energy-looping mechanism employed by these materials allows them to bypass weak GSA transitions in favor of strong ESA transitions, a concept that has not been leveraged for biological imaging. Although energy looping has been observed in bulk[24,39,40] and nanoscale materials,[25−27] it has not been exploited as a method for broadening the range of wavelengths that can be used to excite

DOI: 10.1021/acsnano.6b03288
ACS Nano 2016, 10, 8423−8433

colloidal nanoparticles doped with lanthanide ions. Energy looping may have been overlooked due to its association with photon avalanche. Looping, however, is generally more compatible with biological imaging since it does not require the long induction times, extreme powers, or cryogenic temperatures needed for PA.[23]

We anticipate that an entire class of energy-looping systems can be uncovered using our combinatorial and theoretical approaches. From a purely statistical perspective, the probability of finding a resonant ESA transition in a lanthanide ion with N manifolds is a factor of $\sim N/2$ greater than finding a resonant GSA transition, since there are $(N-1)(N-2)/2$ ESA transitions and only $N-1$ GSA transitions. Since the critical feature in looping is the cross-relaxation step that amplifies a strong-absorbing intermediate state, the high-throughput theoretical screening presented offers a powerful strategy for identifying lanthanide systems with energy levels that host strong ESA in conjunction with a population-multiplying CR step. In combination with experimental validation, our high-throughput pipeline can be extended to target ELNPs excited at additional laser lines in the NIR-II and other windows, *e.g.*, at 1310, 1650, and 1850 nm.

The Tm^{3+}-doped ELNPs reported here are specifically designed to leverage the lower energy and tissue absorption of 1064 nm light, substantially reducing phototoxicity and sample heating. This is a significant design feature since the high excitation power densities required for energy looping and confocal microscopy (10^4–10^6 W/cm^2) would otherwise prohibit the application of ELNPs to biological imaging if using ultraviolet or visible excitation. In addition to the cell viability experiments and live cell imaging reported here, the compatibility of high intensity, 1064 nm excitation (10^6 W/cm^2) with biological samples has been demonstrated by others through the optical trapping of red blood cells in live mice[7] and by the *ex vivo* observation of neuronal growth[50] and cell division[8] in optical traps. The powers utilized here for cell and tissue imaging of ELNPs are also substantially lower than the 10^{11}–10^{12} W/cm^2 peak powers commonly used for *in vivo* multiphoton imaging with NIR pulsed lasers.[1] Thus, the wavelength and fluence of the 1064 nm light used to excite Tm^{3+}-doped ELNPs are compatible with a diverse range of biological imaging applications.

Imaging in live cells and tissue will benefit from additional reduction in photon dose, which can be realized through enhancements in ELNP brightness and lower looping threshold powers. ELNP emission intensities may be increased through rational design of energy transfer in complex heterostructures, by optimizing dopant concentrations for high excitation power densities,[51] by codoping with multiple ions,[13] or by sensitization with organic dyes.[52] In-depth photophysical analysis will increase the fundamental understanding of the mechanisms that support the looping process, directing exploration toward structures that limit the loss of energy from the ESA-CR cycle (Figure 4). Brighter luminescence and lower looping thresholds will reduce the need for high excitation fluxes, although current threshold powers around 10^4 W/cm^2 are already in the range commonly used for confocal imaging, optical trapping, and single nanoparticle microscopy.[18]

Even without these improvements, the ELNPs reported here still exhibit sufficient intensity to be imaged effectively through 1 mm of highly scattering tissue and within cells. In comparison, scattering discourages imaging in tissue at depths >150 μm with visible light[6] and >500 μm with NIR-I light[48] (confirmed by confocal imaging in this work using 785 nm excitation). Imaging ELNPs in cells will be important for witnessing real-time flux of cellular analytes at the single cell level. Tailoring their surface conjugation will facilitate their use as live cell reporters or tumor resection imaging probes. Future studies in three-dimensional cell culture and animal model systems will prove to be the next step in deep brain imaging using ELNPs excited at NIR-II wavelengths. ELNPs will provide opportunities to interrogate more fully the provocative questions about the brain and permit answers to emerge concerning the relationship between neural homeostasis, injury, and disease. Beyond upconversion imaging, energy looping may also prove useful for sensitizing downconversion and for activating biological processes, such as the release of therapeutic agents or optogenetic stimulation of neurons.[52]

CONCLUSION

We have used an energy-looping mechanism to nonresonantly excite upconversion in Tm^{3+}-doped $NaYF_4$ nanoparticles with 1064 nm light. We uncovered these compositions and their underlying mechanisms through high-throughput computational screening based on Judd–Ofelt theory and semiempirical energy-transfer models. The computationally derived energy-looping mechanism was supported by the experimental dependence of the intensity on the excitation power and Tm^{3+} concentration. The minimal absorption of 1064 nm light by fixed mammalian cells enabled confocal imaging with no detectable autofluorescence, using a common cw laser that until now has not been leveraged for luminescence imaging of biological specimens. We used the ability to excite these ELNPs at nonscattering wavelengths to image as deep as 1 mm into tissue-mimicking phantoms and brain tissue. At these thicknesses, the phantoms and tissue attenuated the collected upconversion luminescence signal 5- to 13-fold less than state-of-the-art UCNPs excited at 785 nm. These ELNP particles thus enable the observation of *ca.* 2 μm features millimeters deep in tissue. These feature sizes and imaging depths are comparable to those demonstrated with state-of-the-art multiphoton techniques, with significantly smaller cost and infrastructure. Finally, this mechanism and computational screening strategy can be used to uncover a broader library of ELNP nanoparticles excited at common NIR laser diode wavelengths that have high transmission in brain, porous materials, and other highly scattering media.

METHODS

Materials. Sodium trifluoroacetate, sodium oleate, ammonium fluoride, lanthanide chlorides (99.9+%), oleic acid (OA) (90%), 1-octadecene (ODE) (90%), agarose, Intralipid (IL), 5 μm polystyrene (PS) beads (10% w/v), and phosphate buffer saline (PBS) were purchased from Sigma. Paraformaldehyde was purchased from Electron Microscopy Science.

Synthesis of Core and Core/Shell ELNPs. $NaYF_4$:20% Gd^{3+}, Tm^{3+} particles with diameter $d = 11 \pm 1$ nm were synthesized based on reported procedures[9] and optimized using the Workstation for Automated Nanocrystal Discovery and Analysis (WANDA), a high-throughput robot at the Molecular Foundry.[28] Tm^{3+} was doped from 0.1 to 1.5 at % relative to the total rare-earth content (Y, Gd, Tm).

A 2 nm-thick $NaGdF_4$ shell was grown on selected ELNP cores using a layer-by-layer protocol modified from Li *et al.*[42] and adapted for WANDA as described in Mehra *et al.*[43] Briefly, 6 mL ODE and 4 mL OA were added to the dried ELNP cores and heated to 275 °C in the WANDA glovebox. The automated protocol alternated between

DOI: 10.1021/acsnano.6b03288
ACS Nano 2016, 10, 8423–8433

injections of a 0.2 M sodium trifluoroacetate in OA/ODE (25% v/v) solution and a 0.2 M gadolinium oleate solution in OA/ODE (40% v/v) in a 2:1 mol ratio of sodium to gadolinium precursor. One injection was performed every 15 min for a total of 12 injections (6 injections for each precursor). Following the last injection, each reaction was heated at 275 °C for an additional 30 min and then cooled by nitrogen flow. Core−shell $NaYF_4$ nanoparticles doped with $Nd^{3+}/Yb^{3+}/Ho^{3+}/Gd^{3+}$ (20/10/2/20 at %) were synthesized using analogous methods. Additional synthetic and characterization details are described in the Supporting Information.

Loading NPs into PS Beads. Core−shell NPs were loaded into microbeads[47] (d = 5 μm) by swelling 0.5 mg of PS beads with 250 μL of an 5% v/v chloroform solution in butanol. ELNPs (2 mg in 15 μL hexane) were added to the bead suspension, followed by brief vortexing. After stagnant incubation at 25 °C for 4 h, the beads were washed four times total, alternating between ethanol and cyclohexane. At the end of each wash step, the particles were centrifuged at 4200g for 4 min, except for the last wash, which used 1500g for 2 min.

Confocal Microscopy and Spectroscopy. UCNP emission measurements were performed using a Horiba Jobin Yvon LabRAM ARAMIS confocal microscope with filters purchased from Semrock. ELNPs were excited with a 1064 nm cw laser (MPC) filtered with a 1064 nm laser-line (LL) filter and 980 nm long-pass filter. An 890 nm short pass (SP) filter was used both as a dichroic mirror and as an emission filter. For emission maps of ELNPs, the 800 nm emission peak was integrated between 740 and 870 nm. $NaYF_4$: $Nd^{3+}/Yb^{3+}/Ho^{3+}/Gd^{3+}$ (20/10/2/20 at %) UCNPs with undoped shells were imaged with a 785 nm laser (LaserQuantum) at 10^6 W/cm^2 with spectral acquisition from 450 to 700 nm. The laser was filtered with a 785 nm LL filter (Semrock). A 785 nm SP filter was the dichroic mirror and emission filter. The 540 and 640 nm emission peaks were integrated across ranges of 530−560 nm and 625−675 nm, respectively. Spectral intensities were corrected for the wavelength-dependent instrumental response using a calibrated lamp (Avantes). Average excitation power densities were calculated using measured laser powers and using the $1/e^2$ area calculated from the reflection of the laser spot.

Ligand Removal. ELNPs were rendered hydrophilic for cell studies using a procedure modified from Bogdan *et al.*[44] ELNPs in hexanes were dried in a vial under N_2 flow and dispersed in 0.04 M HCl in 80% ethanol (pH = 1.4) to give a 1 mg/mL solution. After 30 min sonication, 1 mL deionized water was added to the solution and extracted twice against 1.5 mL diethyl ether. Trace diethyl ether in the aqueous layer was removed with gentle N_2 flow. The water-soluble ELNPs were washed with water in a 30 kDa centrifugal filter (Millipore) at 3000g. 120 μL of ligand-stripped ELNPs were retained in the filter at *ca.* 10 mg/mL.

Cell Culture and Microscopy. HeLa cells were maintained in DMEM (Sigma-Aldrich), 10% FBS (Gibco), and 1× penicillin/streptomycin (Sigma-Aldrich) at 37 °C and 5% CO_2. Ibidi μ-Slide VI$^{0.4}$ ibiTreat chambers were coated with 30 μL of 0.2 mg/mL fibronectin (MP Biomedicals) in Dulbecco's PBS (D-PBS) with $CaCl_2$ and $MgCl_2$ (Sigma-Aldrich) to give a 10 μg/cm^2 coating density. Following 20 min incubation at room temperature, chambers were washed twice with 150 μL D-PBS with $CaCl_2$ and $MgCl_2$. Chambers were seeded with 3000 HeLa cells/cm^2 and allowed to attach for 1.5 h at 37 °C and 5% CO_2. Media was carefully removed and replaced with 30 μL of the following reagents in complete DMEM media: *ca.* 140 nM ELNPs (9% (v/v) added ELNP dispersion) or vehicle control. ELNP and vehicle solutions in media were filter sterilized using a 0.22 μm syringe filter (Pall) before treatment of the cells. After an overnight incubation (17 h) at 37 °C and 5% CO_2, cells were washed twice with 150 μL D-PBS with $CaCl_2$ and $MgCl_2$. Cells were fixed with 3.7% formaldehyde (Sigma-Aldrich) in D-PBS with $CaCl_2$ and $MgCl_2$, incubated for 20 min at RT, and washed twice with 150 μL D-PBS with $CaCl_2$ and $MgCl_2$. Fixed cells were imaged with a 1064 nm laser (10^6 W/cm^2) and 50× objective (0.75 NA) with a 50 μm pinhole with 0.35 s acquisition time per pixel at 0.5 μm resolution.

Live Cell Imaging. HeLa cells were maintained in L-15 (Sigma-Aldrich), 10% FBS (Gibco), and 1× penicillin/streptomycin (Sigma-Aldrich) at 37 °C and 100% air. Ibidi μ-Slide I$^{0.4}$ Luer ibiTreat chambers were coated with fibronectin and seeded with 3000 HeLa cells/cm^2. Media was replaced with 200 μL of *ca.* 280 nM ELNPs or 1 μM staurosporine (STS). After overnight incubation at 37 °C, ELNP-treated cells were washed three times with 200 μL complete L-15 media. Confocal imaging was conducted at 25 °C using 1064 nm excitation (10^6 W/cm^2) through a 50× objective (0.75 NA) with a 200 μm pinhole, 0.1 s acquisition time, at 0.75 μm resolution. Following 1064 nm imaging, cells were stained with 3 μg/mL PI in complete L-15 media, then fixed with 3.7% formaldehyde (Sigma-Aldrich) in D-PBS with $CaCl_2$ and $MgCl_2$. Using recorded coordinates of alignment marks, the cell exposed to 1064 nm light was readily identified and imaged on an inverted Zeiss LSM 710 confocal microscope through a 63× oil objective using a 488 nm laser (for autofluorescence) or 514 nm laser (PI).

CellTiter-Glo Viability Assay. Attached HeLa cells were incubated for 17 h in 40 μL vehicle, ELNPs at *ca.* 140 nM, or 1 μM STS (Sigma-Aldrich) in complete DMEM. 40 μL CellTiter-Glo reagent (Promega) was then added to each cell chamber. Chamber contents were mixed and transferred to a 96-well solid-white plate (Corning) for luminescence measurements. To rule out interference from ELNPs, the same procedure was repeated on vehicle and ELNP-treated media without the presence of cells. Complete procedures for cell viability assays and live cell imaging are given in the Supporting Information.

Preparation of Phantoms. IL (0.1−0.5% w/v) was added to a hot solution of agarose in deionized water (1% w/v). Phantoms 0.5−2 mm in thickness were cast between two coverslips separated by spacers of known height. The molten agarose mixtures were injected into these molds and allowed to solidify for 20 min.

Preparation of Mouse Brain Tissue. Animal tissue experiments were performed in accordance with protocols approved by Administrative Panels on Laboratory Animal Care at the University of California, San Francisco and by an Animal Welfare Protocol approved by Lawrence Berkeley National Laboratory. Brain slices were prepared as described previously.[49] Briefly, adult C57BL/6 mice (7−10 weeks old) were anesthetized with isofluorane and decapitated. Using a vibratome (Leica VT1200 S), coronal brain slices were prepared at different thicknesses (ranging from 0.5 and 1 mm, reported before fixation) in a chilled slicing solution consisting of 234 mM sucrose, 11 mM glucose, 24 mM $NaHCO_3$, 2.5 mM KCl, 1.25 mM NaH_2PO_4, 10 mM $MgSO_4$, and 0.5 mM CaCl. Slices were then fixed overnight in 4% paraformaldehyde/1× PBS and then mounted on glass coverslips with a glycerol-based medium (Vectashield, Vector laboratories). Mouse brain transmission spectra were recorded with a collimated beam using an ASD QualitySpec Pro Vis/NIR absorption spectrometer.

Imaging through Phantoms and Brain Slices. ELNP-loaded beads dispersed in ethanol were drop-cast on a silicon substrate and dried to immobilize the beads to the substrate. The silicon substrate was then mounted on a slide with double-sided adhesive tape. A spacer (2 mm) on the slide was used to maintain a <100 μm gap between the beads and the coverslip holding the phantom sample or brain tissue sample. This geometry allowed for imaging of the identical microparticles under different samples. ELNP emission was mapped through phantoms of thickness from 1 to 2 mm, IL concentrations from 0.1% to 0.5%, and brain tissue 0.5 and 1 mm thick. The power density of the 1064 nm excitation was 10^6 W/cm^2. XY maps were acquired with resolution of 0.5−1.0 μm with a 200 μm pinhole and imaged with a 50× 0.5NA objective (Olympus). Integration times ranged from 0.1 to 2 s.

Data Analysis. To compare the intensities of ELNP and UCNP-loaded microbeads, luminescence micrographs were analyzed in ImageJ. Following background subtraction, the integrated intensity of each bead was measured in a circular region of interest around the bead. The signal retention ratio of the phantoms, $S_{phantom}/S_0$, was calculated by dividing the integrated intensity of bead luminescence, $S_{phantom}$, measured through the phantom by the intensity S_0 measured without the phantom.

DOI: 10.1021/acsnano.6b03288
ACS Nano 2016, 10, 8423−8433

ASSOCIATED CONTENT

Supporting Information

The Supporting Information is available free of charge on the ACS Publications website at DOI: 10.1021/acsnano.6b03288.

Additional experimental and theoretical methods, simulation data, X-ray diffraction, vehicle controls, and confocal imaging with 785 nm excitation (PDF)

AUTHOR INFORMATION

Corresponding Author

*E-mail: EMChan@lbl.gov.

Present Address

[∇]Department of Electrical and Computer Engineering, Carnegie Mellon University, Pittsburgh, PA 15213, United States

Author Contributions

[⊥]These authors contributed equally.

Notes

The authors declare no competing financial interest.

ACKNOWLEDGMENTS

The authors thank Jeffrey Urban for helpful conversations. E.S.L. was supported by a SULI internship. This work was performed at the Molecular Foundry and was supported by the Office of Science, Office of Basic Energy Sciences, of the U.S. Department of Energy under contract no. DE-AC02-05CH11231.

REFERENCES

(1) Horton, N. G.; Wang, K.; Kobat, D.; Clark, C. G.; Wise, F. W.; Schaffer, C. B.; Xu, C. In Vivo Three-Photon Microscopy of Subcortical Structures Within an Intact Mouse Brain. *Nat. Photonics* **2013**, *7*, 205−209.

(2) Naczynski, D. J.; Tan, M. C.; Zevon, M.; Wall, B.; Kohl, J.; Kulesa, A.; Chen, S.; Roth, C. M.; Riman, R. E.; Moghe, P. V. Rare-Earth-Doped Biological Composites as in Vivo Shortwave Infrared Reporters. *Nat. Commun.* **2013**, *4*, 2199.

(3) Antaris, A. L.; Chen, H.; Cheng, K.; Sun, Y.; Hong, G.; Qu, C.; Diao, S.; Deng, Z.; Hu, X.; Zhang, B.; Zhang, X.; Yaghi, O. K.; Alamparambil, Z. R.; Hong, X.; Cheng, Z.; Dai, H. A Small-Molecule Dye for NIR-II Imaging. *Nat. Mater.* **2016**, *15*, 235−242.

(4) Welsher, K.; Sherlock, S. P.; Dai, H. Deep-Tissue Anatomical Imaging of Mice Using Carbon Nanotube Fluorophores in the Second Near-Infrared Window. *Proc. Natl. Acad. Sci. U. S. A.* **2011**, *108*, 8943−8948.

(5) Xu, S.; Cui, J.; Wang, L. Recent Developments of Low-Toxicity NIR II Quantum Dots for Sensing and Bioimaging. *TrAC, Trends Anal. Chem.* **2016**, *80*, 149−155.

(6) Hong, G.; Diao, S.; Antaris, A. L.; Dai, H. Carbon Nanomaterials for Biological Imaging and Nanomedicinal Therapy. *Chem. Rev.* **2015**, *115*, 10816−10906.

(7) Zhong, M.-C.; Wei, X.-B.; Zhou, J.-H.; Wang, Z.-Q.; Li, Y.-M. Trapping Red Blood Cells in Living Animals Using Optical Tweezers. *Nat. Commun.* **2013**, *4*, 1768.

(8) Ashkin, A.; Dziedzic, J. M.; Yamane, T. Optical Trapping and Manipulation of Single Cells Using Infrared Laser Beams. *Nature* **1987**, *330*, 769−771.

(9) Ostrowski, A. D.; Chan, E. M.; Gargas, D. J.; Katz, E. M.; Han, G.; Schuck, P. J.; Milliron, D. J.; Cohen, B. E. Controlled Synthesis and Single-Particle Imaging of Bright, Sub-10 Nm Lanthanide-Doped Upconverting Nanocrystals. *ACS Nano* **2012**, *6*, 2686−2692.

(10) Gnach, A.; Lipinski, T.; Bednarkiewicz, A.; Rybka, J.; Capobianco, J. A. Upconverting Nanoparticles: Assessing the Toxicity. *Chem. Soc. Rev.* **2015**, *44*, 1561−1584.

(11) Chen, G.; Qiu, H.; Prasad, P. N.; Chen, X. Upconversion Nanoparticles: Design, Nanochemistry, and Applications in Theranostics. *Chem. Rev.* **2014**, *114*, 5161−5214.

(12) Chan, E. M. Combinatorial Approaches for Developing Upconverting Nanomaterials: High-Throughput Screening, Modeling, and Applications. *Chem. Soc. Rev.* **2015**, *44*, 1653−1679.

(13) Chan, E. M.; Levy, E. S.; Cohen, B. E. Rationally Designed Energy Transfer in Upconverting Nanoparticles. *Adv. Mater.* **2015**, *27*, 5753−5761.

(14) Chan, E. M.; Han, G.; Goldberg, J. D.; Gargas, D. J.; Ostrowski, A. D.; Schuck, P. J.; Cohen, B. E.; Milliron, D. J. Combinatorial Discovery of Lanthanide-Doped Nanocrystals with Spectrally Pure Upconverted Emission. *Nano Lett.* **2012**, *12*, 3839−3845.

(15) Wang, F.; Deng, R.; Wang, J.; Wang, Q.; Han, Y.; Zhu, H.; Chen, X.; Liu, X. Tuning Upconversion Through Energy Migration in Core-Shell Nanoparticles. *Nat. Mater.* **2011**, *10*, 968−973.

(16) Xie, X.; Gao, N.; Deng, R.; Sun, Q.; Xu, Q.-H.; Liu, X. Mechanistic Investigation of Photon Upconversion in Nd 3+-Sensitized Core−Shell Nanoparticles. *J. Am. Chem. Soc.* **2013**, *135*, 12608−12611.

(17) Shen, J.; Chen, G.; Vu, A.-M.; Fan, W.; Bilsel, O. S.; Chang, C.-C.; Han, G. Engineering the Upconversion Nanoparticle Excitation Wavelength: Cascade Sensitization of Tri-Doped Upconversion Colloidal Nanoparticles at 800 Nm. *Adv. Opt. Mater.* **2013**, *1*, 644−650.

(18) Gargas, D. J.; Chan, E. M.; Ostrowski, A. D.; Aloni, S.; Altoe, M. V. P.; Barnard, E. S.; Sanii, B.; Urban, J. J.; Milliron, D. J.; Cohen, B. E.; Schuck, P. J. Engineering Bright Sub-10-Nm Upconverting Nanocrystals for Single-Molecule Imaging. *Nat. Nanotechnol.* **2014**, *9*, 300−305.

(19) Liu, J.; Wu, R.; Li, N.; Zhang, X.; Zhan, Q.; He, S. Deep, High Contrast Microscopic Cell Imaging Using Three-Photon Luminescence of B-(NaYF4:Er3+/NaYF4) Nanoprobe Excited by 1480-Nm CW Laser of Only 15-mW. *Biomed. Opt. Express* **2015**, *6*, 1857.

(20) Zhan, Q.; Qian, J.; Liang, H.; Somesfalean, G.; Wang, D.; He, S.; Zhang, Z.; Andersson-Engels, S. Using 915 Nm Laser Excited Tm3+/Er3+/Ho3+-Doped NaYbF4 Upconversion Nanoparticles for in Vitro and Deeper in Vivo Bioimaging Without Overheating Irradiation. *ACS Nano* **2011**, *5*, 3744−3757.

(21) Burks, P. T.; Garcia, J. V.; GonzalezIrias, R.; Tillman, J. T.; Niu, M.; Mikhailovsky, A. A.; Zhang, J.; Zhang, F.; Ford, P. C. Nitric Oxide Releasing Materials Triggered by Near-Infrared Excitation Through Tissue Filters. *J. Am. Chem. Soc.* **2013**, *135*, 18145−18152.

(22) Brenier, A.; Garapon, C.; Madej, C.; Pédrini, C.; Boulon, G. Dynamics of Looping Mechanisms in Laser Crystals. *Opt. Mater.* **1994**, *4*, 51−54.

(23) Liu, G.; Chen, X. Chapter 233: Spectroscopic Properties of Lanthanides in Nanomaterials. In *Handbook on the Physics and Chemistry of Rare Earths*; Elsevier: Amsterdam, The Netherlands, 2007; Vol. *37*, pp 99−169.

(24) Sivakumar, S.; van Veggel, F. C. J. M.; May, P. S. Near-Infrared (NIR) to Red and Green Up-Conversion Emission From Silica Sol-Gel Thin Films Made with La0.45Yb0.50Er0.05F3 Nanoparticles, Hetero-Looping-Enhanced Energy Transfer (Hetero-LEET): a New Up-Conversion Process. *J. Am. Chem. Soc.* **2007**, *129*, 620−625.

(25) Dwivedi, Y.; Thakur, S. N.; Rai, S. B. Study of Frequency Upconversion in Yb3+/Eu3+ by Cooperative Energy Transfer in Oxyfluoroborate Glass Matrix. *Appl. Phys. B: Lasers Opt.* **2007**, *89*, 45−51.

(26) Mishra, K.; Dwivedi, Y.; Rai, S. B. Observation of Avalanche Upconversion Emission in Pr:Y2O3 Nanocrystals on Excitation with 532 Nm Radiation. *Appl. Phys. B: Lasers Opt.* **2012**, *106*, 101−105.

(27) Deng, H.; Yang, S.; Xiao, S.; Gong, H.-M.; Wang, Q.-Q. Controlled Synthesis and Upconverted Avalanche Luminescence of Cerium(III) and Neodymium(III) Orthovanadate Nanocrystals with High Uniformity of Size and Shape. *J. Am. Chem. Soc.* **2008**, *130*, 2032−2040.

(28) Chan, E. M.; Xu, C.; Mao, A. W.; Han, G.; Owen, J. S.; Cohen, B. E.; Milliron, D. J. Reproducible, High-Throughput Synthesis of

DOI: 10.1021/acsnano.6b03288
ACS Nano 2016, 10, 8423−8433

Colloidal Nanocrystals for Optimization in Multidimensional Parameter Space. *Nano Lett.* **2010**, *10*, 1874−1885.
(29) Chan, E. M.; Gargas, D. J.; Schuck, P. J.; Milliron, D. J. Concentrating and Recycling Energy in Lanthanide Codopants for Efficient and Spectrally Pure Emission: the Case of NaYF4:Er3+/Tm3+ Upconverting Nanocrystals. *J. Phys. Chem. B* **2012**, *116*, 10561−10570.
(30) Liu, Y.; Sonek, G. J.; Berns, M. W.; Tromberg, B. J. Physiological Monitoring of Optically Trapped Cells: Assessing the Effects of Confinement by 1064-Nm Laser Tweezers Using Microfluorometry. *Biophys. J.* **1996**, *71*, 2158−2167.
(31) Walsh, B. M. Judd−Ofelt Theory: Principles and Practices. In *Advances in Spectroscopy for Lasers and Sensing*; Di Bartolo, B.; Forte, O., Eds.; Springer: Amsterdam, The Netherlands, 2006; pp 400−433.
(32) Mor, F. M.; Sienkiewicz, A.; Forró, L.; Jeney, S. Upconversion Particle as a Local Luminescent Brownian Probe - a Photonic Force Microscopy Study. *ACS Photonics* **2014**, *1*, 1251−1257.
(33) Ivanova, S. E.; Tkachuk, A. M.; Mirzaeva, A.; Pelle, F. Spectroscopic Study of Thulium-Activated Double Sodium Yttrium Fluoride Na0.4Y0.6F2.2: Tm3+ Crystals: I. Intensity of Spectra and Luminescence Kinetics. *Opt. Spectrosc.* **2008**, *105*, 228−241.
(34) Peterka, P.; Kasik, I.; Dhar, A.; Dussardier, B.; Blanc, W. Theoretical Modeling of Fiber Laser at 810 Nm Based on Thulium-Doped Silica Fibers with Enhanced 3H4 Level Lifetime. *Opt. Express* **2011**, *19*, 2773−2781.
(35) Hanna, D. C.; Percival, R. M.; Perry, I. R.; Smart, R. G.; Townsend, J. E.; Tropper, A. C. Frequency Upconversion in Tm- and Yb:Tm-Doped Silica Fibers. *Opt. Commun.* **1990**, *78*, 187−194.
(36) Fujiwara, H.; Sasaki, K. Upconversion Lasing of a Thulium-Ion-Doped Fluorozirconate Glass Microsphere. *J. Appl. Phys.* **1999**, *86*, 2385.
(37) Wang, F.; Han, Y.; Lim, C. S.; Lu, Y.; Wang, J.; Xu, J.; Chen, H.; Zhang, C.; Hong, M.; Liu, X. Simultaneous Phase and Size Control of Upconversion Nanocrystals Through Lanthanide Doping. *Nature* **2010**, *463*, 1061−1065.
(38) Goldner, P.; Pelle, F. Photon Avalanche Fluorescence and Lasers. *Opt. Mater.* **1996**, *5*, 239−249.
(39) Joubert, M. F. Photon Avalanche Upconversion in Rare Earth Laser Materials. *Opt. Mater.* **1999**, *11*, 181−203.
(40) Chivian, J. S.; Case, W. E.; Eden, D. D. The Photon Avalanche: a New Phenomenon in Pr3+-Based Infrared Quantum Counters. *Appl. Phys. Lett.* **1979**, *35*, 124.
(41) Homan, K.; Kim, S.; Chen, Y.-S.; Wang, B.; Mallidi, S.; Emelianov, S. Prospects of Molecular Photoacoustic Imaging at 1064 Nm Wavelength. *Opt. Lett.* **2010**, *35*, 2663.
(42) Li, X.; Shen, D.; Yang, J.; Yao, C.; Che, R.; Zhang, F.; Zhao, D. Successive Layer-by-Layer Strategy for Multi-Shell Epitaxial Growth: Shell Thickness and Doping Position Dependence in Upconverting Optical Properties. *Chem. Mater.* **2013**, *25*, 106−112.
(43) Mehra, S.; Chan, E. M.; Salleo, A. Modular Synthetic Design Enables Precise Control of Shape and Doping in Colloidal Zinc Oxide Nanorods. *J. Mater. Chem. C* **2015**, *3*, 7172−7179.
(44) Bogdan, N.; Vetrone, F.; Ozin, G. A.; Capobianco, J. A. Synthesis of Ligand-Free Colloidally Stable Water Dispersible Brightly Luminescent Lanthanide-Doped Upconverting Nanoparticles. *Nano Lett.* **2011**, *11*, 835−840.
(45) Nam, S. H.; Bae, Y. M.; Park, Y. I.; Kim, J. H.; Kim, H. M.; Choi, J. S.; Lee, K. T.; Hyeon, T.; Suh, Y. D. Long-Term Real-Time Tracking of Lanthanide Ion Doped Upconverting Nanoparticles in Living Cells. *Angew. Chem., Int. Ed.* **2011**, *50*, 6093−6097.
(46) Caterina, M. J.; Schumacher, M. A.; Tominaga, M.; Rosen, T. A.; Levine, J. D.; Julius, D. The Capsaicin Receptor: a Heat-Activated Ion Channel in the Pain Pathway. *Nature* **1997**, *389*, 816−824.
(47) Han, M.; Gao, X.; Su, J. Z.; Nie, S. Quantum-Dot-Tagged Microbeads for Multiplexed Optical Coding of Biomolecules. *Nat. Biotechnol.* **2001**, *19*, 631−635.
(48) Dunn, A. K.; Wallace, V. P.; Coleno, M.; Berns, M. W.; Tromberg, B. J. Influence of Optical Properties on Two-Photon Fluorescence Imaging in Turbid Samples. *Appl. Opt.* **2000**, *39*, 1194−1201.
(49) Gee, S.; Ellwood, I.; Patel, T.; Luongo, F.; Deisseroth, K.; Sohal, V. S. Synaptic Activity Unmasks Dopamine D2 Receptor Modulation of a Specific Class of Layer v Pyramidal Neurons in Prefrontal Cortex. *J. Neurosci.* **2012**, *32*, 4959−4971.
(50) Mohanty, S. K.; Sharma, M.; Panicker, M. M.; Gupta, P. K. Controlled Induction, Enhancement, and Guidance of Neuronal Growth Cones by Use of Line Optical Tweezers. *Opt. Lett.* **2005**, *30*, 2596−2598.
(51) Zhao, J.; Jin, D.; Schartner, E. P.; Lu, Y.; Liu, Y.; Zvyagin, A. V.; Zhang, L.; Dawes, J. M.; Xi, P.; Piper, J. A.; Goldys, E. M.; Monro, T. M. Single-Nanocrystal Sensitivity Achieved by Enhanced Upconversion Luminescence. *Nat. Nanotechnol.* **2013**, *8*, 729−734.
(52) Wu, X.; Zhang, Y.; Takle, K.; Bilsel, O.; Li, Z.; Lee, H.; Zhang, Z.; Li, D.; Fan, W.; Duan, C.; Chan, E. M.; Lois, C.; Han, G. Dye-Sensitized Core/Active Shell Upconversion Nanoparticles for Optogenetics and Bioimaging Applications. *ACS Nano* **2016**, *10*, 1060−1066.

DOI: 10.1021/acsnano.6b03288
ACS Nano 2016, 10, 8423−8433